Smart Agricultural Technology 13 (2026) 101846

Contents lists available at ScienceDirect

Smart Agricultural Technology

journal homepage: www.journals.elsevier.com/smart-agricultural-technology

Adaptive GNSS–UWB sensor fusion for reliable localization in precision agriculture

Anas Osman [a,b], Farhad Shamsfakhr [a], Massimo Vecchio [a,*], Fabio Antonelli [a]

[a] Fondazione Bruno Kessler (FBK), Trento, Italy
[b] Doctorate Program in Industrial Innovation, University of Trento, Italy

ARTICLE INFO

Keywords:
Extended Kalman filter (EKF)
Multi-sensor fusion
RTK
GNSS–UWB fusion
Non-Line-of-Sight (NLOS) mitigation
Adaptive covariance estimation
Agricultural robotics

ABSTRACT

Accurate and reliable localization is essential for precision agriculture, where operations such as autonomous navigation, mapping, and agriculture-oriented applications demand centimeter- or even sub-centimeter accuracy. However, satellite-based systems, whether ground-corrected or not, often experience reduced performance in agricultural settings due to canopy cover, multi-path, and Non-Line-of-Sight (NLOS) conditions. This paper presents an adaptive sensor fusion framework that integrates GNSS and Ultra-Wideband (UWB) ranging within an Extended Kalman Filter (EKF). The proposed method explicitly models UWB bias under NLOS, introduces a GNSS health score based on raw measurements and estimates acquired by the receiver for data-driven covariance adaptation, and employs a learning-based approach to tune UWB measurement uncertainty dynamically. Experimental validation in agricultural field settings demonstrates that the adaptive EKF achieves centimeter-level accuracy in open-sky conditions and maintains 2D horizontal RMSE below 6 cm in the partially obstructed (NLOS) field tests, outperforming standard fusion approaches by more than 40% in RMSE. The results demonstrate the potential of adaptive multi-sensor fusion to deliver robust and cost-effective localization for agricultural automation.

1. Introduction

Accurate localization is a cornerstone of precision agriculture. Modern farming increasingly relies on automated machinery, variable rate technologies, and site-specific management, all of which depend on the ability to determine position with high accuracy and reliability. Unlike generic navigation tasks, agricultural operations are characterized by repetitive field patterns, long working hours, and environments where even small localization errors can accumulate into significant inefficiencies or crop damage [1].

The required accuracy varies depending on the specific agricultural task. At the lower end of the precision spectrum, yield mapping and soil sampling can tolerate accuracies in the range of 20–50 cm, as the primary goal is to georeference data across campaigns consistently [2]. Progressing to more demanding applications, autonomous tractor guidance demands decimeter-level precision to maintain consistent lane keeping and prevent overlaps or gaps between passes, though only a few proprietary solutions currently provide reliable performance [3]. Even tighter tolerances, in the sub-decimeter range, are needed for tasks such as row-crop planting and mechanical weeding, as well as for SLAM-based fruit-tree localization [4]. Although not always explicitly documented, these requirements can be met using modern Real-Time Kinematics (RTK) systems [5]. At the highest precision tier, operations such as robotic harvesting or targeted spraying necessitate sub-centimeter localization accuracy. Early studies demonstrated the feasibility of such performance, with vision-based micro-dosing systems achieving sub-centimeter application accuracy [6]. Comparable results have since been reported for robotic harvesting, where recent advances in visual-servoing systems have achieved mean end-effector positioning errors as low as 0.5 cm [7]. For a broader overview of sub-centimeter solutions in agricultural robotics, readers may refer to [8] and the references therein.

Meeting these requirements in real agricultural environments is challenging. Modern satellite navigation systems enable users to determine their position anywhere on Earth and represent the default technology for outdoor positioning. However, their performance is often degraded on farms due to multipath effects, canopy obstruction, and intermittent Non-Line-of-Sight (NLOS) conditions caused by tall crops, agricultural machinery, or surrounding structures [9,10]. These degradations can introduce errors ranging from a few centimeters to several meters, which exceed the acceptable thresholds reported in Table 1.

* Corresponding author.
E-mail addresses: aosman@fbk.eu (A. Osman), fshamsfakhr@gmail.com, fshamsfakhr@fbk.eu (F. Shamsfakhr), mvecchio@fbk.eu (M. Vecchio), fantonelli@fbk.eu (F. Antonelli).

https://doi.org/10.1016/j.atech.2026.101846
Received 20 November 2025; Received in revised form 18 January 2026; Accepted 27 January 2026
Available online 29 January 2026
2772-3755/© 2026 Published by Elsevier B.V. This is an open access article under the CC BY-NC-ND license (http://creativecommons.org/licenses/by-nc-nd/4.0/).

Table 1
State-of-the-art positioning accuracy for different agricultural operations, from low-precision mapping to high-precision interventions.

Operation	Accuracy	Reference
Yield mapping and soil sampling	20–50 cm	[2]
Autonomous tractor guidance	5–10 cm	[3]
Row-crop planting, weeding, fruit-tree localization	2–5 cm	[4,5]
Targeted spraying, robotic harvesting	< 1 cm	[6,7]

In addition, unlike urban or industrial contexts, agricultural environments are characterized by highly dynamic and season-dependent conditions: crop canopy evolves throughout the growing season, machinery introduces metallic obstructions that amplify multipath, and temporary infrastructures (*e.g.*, irrigation systems, overhead agrivoltaics) further reduce satellite visibility [11]. This variability makes it difficult to rely solely on satellite-based localization, even when corrections from ground-based services such as RTK or PPP are applied [15], since signal outages or local interference can rapidly degrade performance. In recent precision agriculture experiments, RTK achieved accuracies of just a few centimeters in favorable conditions, but errors increased to over 20 cm in obstructed settings. Similarly, PPP corrections provided accuracies below 10 cm in open sky, yet deteriorated to more than half a meter under canopy cover [16].

To address these limitations, recent studies have increasingly investigated multi-sensor fusion approaches, combining satellite positioning with low-cost inertial measurement units (IMUs), vision-based systems, Ultra-Wideband (UWB) ranging, or LiDAR sensors [4]. These methods aim to enhance accuracy and robustness under degraded signal conditions, while maintaining costs compatible with agricultural applications [17]. Following this direction, the present work explores the integration of satellite localization and UWB in agricultural environments, intending to provide a reliable positioning solution that meets the accuracy requirements of precision farming. Specifically, this paper makes the following contributions:

1. Design of an adaptive, data-driven method to estimate and update measurement covariances for GNSS and UWB within a Kalman-filter fusion scheme.
2. Mapping a unified GNSS health score to time-varying GNSS covariance via calibrated inflation.
3. Experimental validation in agricultural-like conditions with RTK baseline, UWB anchors, and mixed LOS/NLOS trajectories.
4. Demonstration of $>40\%$ RMSE reduction over standard EKF, achieving 5–10 cm 2D horizontal accuracy under NLOS conditions, while preserving centimeter-level performance in LOS.

While Table 1 summarizes accuracy requirements across agricultural operations, state-of-the-art localization still degrades markedly under canopy and multipath. The proposed adaptive GNSS–UWB fusion directly targets these gaps by dynamically down-weighting degraded signals and modeling UWB NLOS bias, delivering resilience that aligns with the accuracy needs of advanced agricultural automation.

The remainder of this paper is organized as follows. Section 2 reviews related work on outdoor localization degradation and multi-sensor fusion in agricultural environments. Then, Section 3 describes the system models, while Section 4 introduces the proposed outdoor localization–UWB fusion framework and its implementation details. Section 5 describes the experimental setup and scenarios, while Section 6 reports the results and comparative evaluation. Finally, Section 7 concludes the paper and outlines future research directions.

2. Related works

Global Navigation Satellite Systems (GNSS), particularly GPS, remain the dominant method for localization in precision agriculture. Robot-mounted receivers without correction exhibit variations of 0.6–5 m depending on the environment [18]. Performance deteriorates sharply in orchards and dense row crops, where multipath and canopy attenuation are common, with reported errors ranging from 0.02–0.62 m under canopy [19,20].

When corrections are applied, localization accuracy improves significantly. Local RTK, which relies on a nearby ground reference station transmitting real-time correction data to the rover, can provide accuracies of about 4.5 cm under open-sky conditions. In contrast, global correction services such as Trimble SF3 and SF1 achieve approximately 8.5 cm and 11.5 cm, respectively, at 95% confidence [21]. However, these services are affected by correction signal outages in remote areas, adverse weather, and anomalies such as the South Atlantic Magnetic Anomaly (SAMA), which can degrade reliability in the Southern Hemisphere [22].

These limitations confine satellite-based localization to favorable field conditions and highlight the need for complementary sensing solutions. To overcome these challenges, multi-source sensor aggregation and fusion techniques are increasingly employed to integrate heterogeneous sensors and compensate for individual weaknesses. By combining absolute positioning systems (*e.g.*, GNSS) with relative (*e.g.*, UWB), inertial (*e.g.*, IMU), vision-based (*e.g.*, RGB, stereo cameras), and environmental sensing (*e.g.*, LiDAR) technologies, it is possible to enhance robustness, reduce drift, and maintain localization accuracy under adverse conditions such as canopy occlusion or signal loss.

Among the explored strategies, fusing IMU data with LiDAR measurements has been investigated for orchard and row navigation. Extended Kalman Filters (EKF) increase the distance of intervention-free navigation from 50 (LiDAR only) to 400 m in open fields, and from 16 to 56 m in production settings [22]. While effective for heading and lateral distance estimation, LiDAR-based systems remain costly and sensitive to dust, rain, and canopy geometry. Simultaneous Localization and Mapping (SLAM) methods further extend capabilities in GNSS-degraded environments by combining GNSS and exteroceptive sensing to reduce pose and map errors [4,23,24]. Semantic and hybrid topological-metric mapping frameworks improve long-range navigation but suffer from accumulated drift and reliance on dense features, limiting scalability to large or uniform fields.

Fusing GNSS and IMU data provides another solution, often aided by non-holonomic constraints (NHC) or dual-antenna configurations. This reduces drift during outages by over 80% and stabilizes azimuth, achieving lateral errors of 3 mm and heading errors below 0.03° under continuous GNSS coverage [18]. Yet, performance deteriorates during prolonged outages, and dual-antenna setups add complexity and cost [22].

In recent studies, researchers have made significant strides in sensor fusion by using raw GNSS observations like pseudo-range, Doppler, and carrier phase directly instead of relying on pre-processed GNSS fixes. Prominent examples include works by [25–28], which demonstrate tightly coupled systems. These systems successfully fuse GNSS raw measurements into factor graph optimization frameworks, incorporating data from LiDAR or visual-inertial sources. Even though these methods are robust, their accuracy largely hinges on environmental conditions. In optimal scenarios, their error margins are around 25 cm, but they can increase to over a meter in tough urban environments.

Approaches combining vision sensors and GNSS have also gained attention, as they can leverage semantic keypoints, meta-learning, and deep models for crop-row detection. CropFollow++ and MetaCropFollow demonstrated robustness under canopy conditions [19,20], while deep learning models for object detection (*e.g.*, YOLOv3) enabled real-time row detection without costly hardware [24]. These approaches provide cost-effective implementation and semantic awareness but remain sensitive to lighting variations, foliage occlusion, and computational demands on embedded platforms.

UWB technology has recently emerged as a promising complement to GNSS. Fusion approaches reduce positioning error from about 2 m to below 40 cm [29], while machine learning methods further decrease

Table 2
Comparison of localization approaches in agricultural environments, with the proposed method highlighted in gray.

Method	Typical Accuracy	Advantages	Limitations
GNSS (Local RTK, SF1/SF3, NLOS RTK, No RTK)	4.5–22.5 cm; 8.5–65.5 cm; 11.5–25.5 cm; 0.02–0.62 m; open-sky: 0.6–5 m [18,21]	Mature, low-cost, widely adopted	Multipath, canopy attenuation, weather, SAMA
LiDAR–IMU Fusion	Cm-level lateral accuracy for up to 400 m in open fields, 56 m in orchards [4,22]	Accurate heading; drift reduction	Expensive; sensitive to dust, rain, canopy
GNSS–IMU Fusion	Few cm lateral error; heading <0.1°; drift reduced >80% during outages [18,22]	Stabilizes azimuth; reduces drift; robust during short outages	Accuracy degrades in prolonged GNSS outages; higher system cost
Raw GNSS Fusion (Factor Graphs, Tightly Coupled)	~0.25 m in open-sky; >1 m in urban environments [26,28]	Incorporates pseudo-range, Doppler, carrier phase; robust factor graph optimization with LiDAR or visual-inertial integration	Accuracy strongly environment-dependent; degraded in multipath-rich areas
Vision / SLAM (Row-following, Mapping)	Lateral error ~10 cm (orchards) [20]; pose error 5–20 cm (field SLAM) [24]	Low-cost cameras; semantic cues; robust in GNSS-denied areas	Sensitive to lighting/occlusion; drift accumulates
UWB (Standalone)	Typical: 10–30 cm [34]; optimized: 4–6 cm [33]	Indoor/outdoor use; ML improves robustness [12,13]; robust filtering [14]	Needs anchors; infrastructure cost; static bias modeling
GNSS–UWB Fusion	Drift reduced from 2.1 m to <40 cm [29]; mean error 0.16 m (RMSE 0.18 m) with ML-based fusion [30]	Seamless GNSS resilience; robust indoor–outdoor transitions	Still GNSS-dependent; added system complexity

mean error to 0.16 m and enable seamless indoor–outdoor transitions [30]. Autoencoder-based novelty detection mitigates NLOS errors by up to 60% [31], multipath mapping with Least-Squares Collocation reduces RMSE by 13–16% [32], and optimization-based Interactive Time of Arrival (ITOA) schemes achieve 4–6 cm accuracy under dynamic agricultural conditions [33]. Recent UWB-specific NLOS identification and mitigation methods have also been proposed [12–14]. These works emphasize learning-based NLOS detection and error mitigation at the UWB ranging/positioning level [12,13], as well as robust filtering strategies when UWB is integrated with inertial sensing [14]. In contrast, our focus is on outdoor precision-agriculture operation and adaptive GNSS–UWB fusion, where GNSS quality is explicitly monitored and the EKF measurement covariance is tuned online while estimating and compensating UWB NLOS bias within the filter. Nonetheless, existing methods largely rely on fixed weighting strategies and overlook explicit modeling of UWB bias or GNSS signal quality.

Despite these advances, existing approaches often degrade under canopy, incur high costs, or lack adaptability in dynamic field conditions. To overcome these limitations, this work introduces an adaptive GNSS–UWB fusion framework that augments the EKF state with a dedicated UWB bias term and dynamically adjusts measurement covariances based on signal quality. The proposed method achieves centimeter-level accuracy in LOS and 2D horizontal RMSE below 6 cm under NLOS, as highlighted in the last row of Table 2, which summarizes representative localization methods, their reported accuracy, advantages, and limitations in agricultural environments.

3. System models

This section introduces the mathematical models describing the robot dynamics and the measurement processes of the UWB and GNSS-RTK systems, which form the basis for the proposed localization framework.

3.1. Robot motion

Consider a ground vehicle whose body-x axis is aligned with its forward direction. Let the robot state be

$$s(t) = \begin{bmatrix} \boldsymbol{p}(t) \\ \boldsymbol{\eta}(t) \end{bmatrix} = \begin{bmatrix} x & y & z & \rho & \phi & \theta \end{bmatrix}^\top, \tag{1}$$

where $\boldsymbol{p} = [x, y, z]^\top$ is the position in the world frame $\langle W \rangle$, and $\boldsymbol{\eta} = [\rho, \phi, \theta]^\top$ are roll, pitch, and yaw (ZYX convention). Let $R(\boldsymbol{\eta}) \in SO(3)$ be the rotation from body $\langle B \rangle$ to world $\langle W \rangle$. The body-frame inputs are the forward (body-x) speed v and the angular velocity $\boldsymbol{\omega} = [p, q, r]^\top$ (roll/pitch/yaw rates), available from proprioceptive sensors and assumed piecewise constant over a sampling period T_s. Under a standard kinematic (no-slip) model, we denote $s_{k+1} = s((k+1)T_s) = [\boldsymbol{p}_{k+1}^\top, \boldsymbol{\eta}_{k+1}^\top]^\top$ and assume v and $\boldsymbol{\omega}$ remain constant over the interval $[kT_s, (k+1)T_s)$. Under these assumptions, the following discrete-time equivalent dynamics can be derived, as visualized in Fig. 1.

for (1):

$$\begin{aligned} \boldsymbol{p}_{k+1} &= \boldsymbol{p}_k + R(\boldsymbol{\eta}_k)\, J(\boldsymbol{\omega}_k T_s) \begin{bmatrix} v_k \\ 0 \\ 0 \end{bmatrix}, \\ \boldsymbol{\delta p}_k &= R(\boldsymbol{\eta}_k)\, J(\boldsymbol{\omega}_k T_s) \begin{bmatrix} v_k \\ 0 \\ 0 \end{bmatrix}, \\ R(\boldsymbol{\eta}_{k+1}) &= R(\boldsymbol{\eta}_k)\, \Delta R_k. \end{aligned} \tag{2}$$

where $\Delta R_k = \exp(\Omega_k T_s) \in SO(3)$ is the incremental rotation, and Ω_k is the skew-symmetric matrix of $\boldsymbol{\omega}_k$ as follows:

$$\Omega_k = \begin{bmatrix} 0 & -r_k & q_k \\ r_k & 0 & -p_k \\ -q_k & p_k & 0 \end{bmatrix}, \qquad \|\boldsymbol{\omega}_k\| = \omega_k. \tag{3}$$

and $J(\boldsymbol{\omega}_k T_s)$ is the SO(3) left Jacobian :

$$J(\boldsymbol{\omega}_k T_s) = I_3 - \frac{1 - \cos(\omega_k T_s)}{\omega_k^2}\, \Omega_k + \frac{\omega_k T_s - \sin(\omega_k T_s)}{\omega_k^3}\, \Omega_k^2. \tag{4}$$

Moreover, we notice that when $\omega_k \to 0$, $J(\boldsymbol{\omega}_k T_s) \to I_3$, giving

$$\boldsymbol{p}_{k+1} = \boldsymbol{p}_k + R(\boldsymbol{\eta}_k) \begin{bmatrix} v_k T_s \\ 0 \\ 0 \end{bmatrix}, \quad R(\boldsymbol{\eta}_{k+1}) = R(\boldsymbol{\eta}_k). \tag{5}$$

3.2. UWB ranging

In our case, UWB range measurements are modeled using the Time-of-Arrival (TOA) principle. A signal emitted at time t_0 is received at time $t_0 + \tau$, and the corresponding propagation delay τ is converted into distance by multiplying by the wave speed c. This provides a direct estimate of the geometric distance between the rover-mounted UWB tag and each fixed anchor, later corrupted by measurement noise and possible NLOS-induced biases.

Therefore,

$$TOA = t_0 + \tau + \epsilon_t = t_0 + \frac{\rho_{i,k}}{c} \quad \Longleftrightarrow \quad \rho_{i,k} = c\,(\tau + \epsilon_t), \tag{6}$$

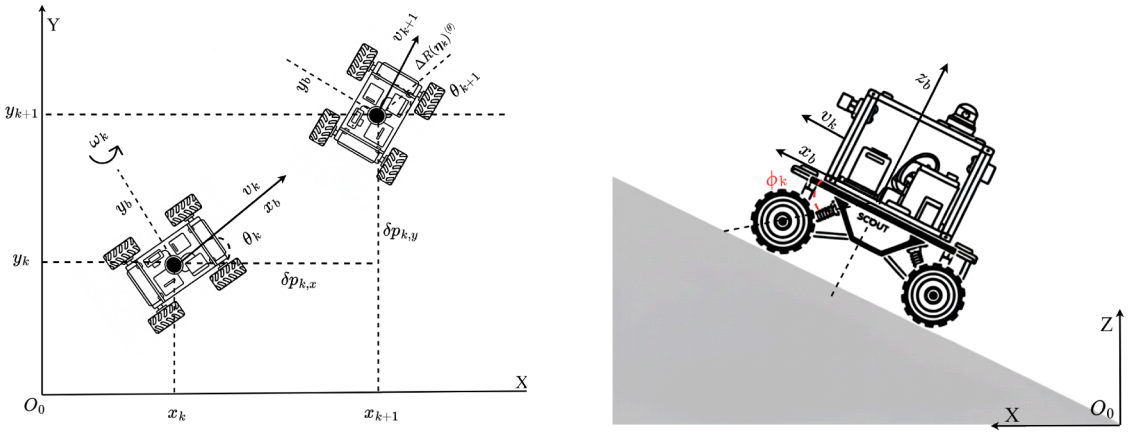

(a) Planar kinematic model of the rover in the $X-Y$ frame. The rover's forward velocity v_k is aligned with the body x_b-axis, while the yaw angle θ_k defines its orientation with respect to the global frame. The motion update between steps k and $k+1$ is expressed by the position increments $\delta p_{k,x}, \delta p_{k,y}$ and the rotation update $\Delta R(\eta_k^{(\theta)})$.

(b) Rover kinematic model on an inclined plane in the $X-Z$ frame. The rover velocity v_k is aligned with the body axis x_b, while the body frame $\{x_b, z_b\}$ is rotated with respect to the global frame $\{X, Z\}$ by the slope angle ϕ_k. This pitch angle ϕ_k captures the effect of the terrain inclination on the rover dynamics.

Fig. 1. Rover kinematic models: (a) planar motion in the $X-Y$ frame and (b) inclined-plane motion in the $X-Z$ frame.

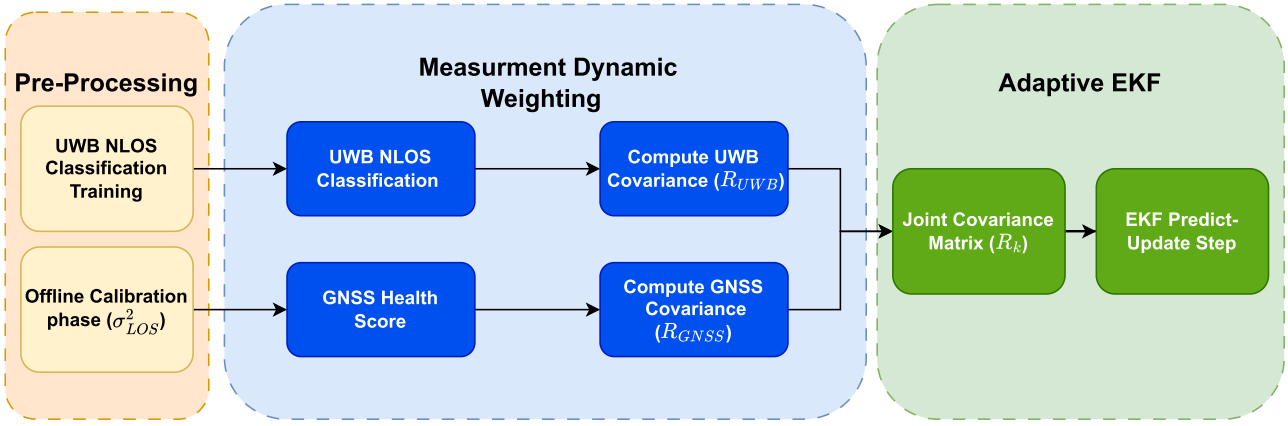

Fig. 2. The framework consists of an offline calibration phase, where GNSS parameters are calibrated and a UWB NLOS classification network is trained, and an online filtering loop, which dynamically adjusts measurement covariances based on GNSS quality and UWB NLOS scores to improve state estimation accuracy.

and it follows that the range error can be expressed as $\rho_{i,k} - c\,\tau = c\,\epsilon_t$, where the uncertainty is induced by the time-stamping error ϵ_t.

Assume the environment is instrumented with m UWB anchors at known coordinates (X_i, Y_i, Z_i) in $\langle W \rangle$. Let $\bar{z}_{i,k}$ denote the geometric distance between the robot-mounted UWB tag, located at $\boldsymbol{p}_k$, and anchor i at time kT_s:

$$\bar{z}_{i,k} = \sqrt{(X_i - x_k)^2 + (Y_i - y_k)^2 + (Z_i - z_k)^2}. \tag{7}$$

ToA measurements are affected by zero-mean white noise $\varepsilon_{i,k}$ and, under NLOS conditions, by a positive additive offset $o_{i,k} > 0$, which is unknown and assumed piecewise-constant. Accordingly, the measured range is given by

$$z_{i,k} = \bar{z}_{i,k} + o_{i,k} + \varepsilon_{i,k}. \tag{8}$$

3.3. GNSS-RTK measurement

Let the rover position at epoch k be denoted as $\mathbf{p}_k^r = [x_k^r, y_k^r, z_k^r]^\top \in \mathbb{R}^3$, and let the reference station position be known as $\mathbf{p}_{\text{base}} = [x^b, y^b, z^b]^\top$. For satellite $\mathbf{s}$ with ECEF coordinates $\mathbf{s}_k^{\mathbf{s}} = [X_k^{\mathbf{s}}, Y_k^{\mathbf{s}}, Z_k^{\mathbf{s}}]^\top$, At each epoch k, the rover and the base station simultaneously record pseudorange and carrier-phase measurements from the same set of satellites. These raw observations include the true geometric ranges together with satellite clock errors, atmospheric delays, hardware biases, and measurement noise. By forming double-differences between rover–base and satellite pairs, most common errors are removed, leaving primarily the rover–base relative vector and the carrier-phase integer ambiguities. Once these ambiguities are resolved (fixed RTK), the baseline between rover and base can be estimated with centimeter-level precision. Finally, the rover's position is obtained as the sum of the known base position,

the estimated relative displacement, residual biases, and measurement noise:

$$\hat{\mathbf{p}}_k = \mathbf{p}_{\text{base}} + \Delta\mathbf{p}_{\text{true},k} + \mathbf{b}_k + \boldsymbol{\epsilon}_k,$$

where $\mathbf{p}_{\text{base}}$ denotes the known (fixed) base station position, $\Delta\mathbf{p}_{\text{true},k}$ is the true relative vector from the base to the rover at epoch k, $\mathbf{b}_k$ represents the residual systematic biases (*e.g.*, atmospheric delays, orbit errors, multipath, hardware offsets) that are not fully canceled, and $\boldsymbol{\epsilon}_k$ denotes the random measurement noise.

4. Problem formulation

Building upon the system models, this section formulates the localization problem under degraded measurement conditions and presents the adaptive estimation strategies integrated into the EKF framework as seen in Fig. 2.

4.1. GNSS health score and covariance estimation

We define a GNSS *health score* $\alpha_{\text{GNSS},k} \in [0,1]$ that aggregates multiple quality indicators into a single metric. Based on this score, a scalar *penalty weight* $\omega_G \geq 0$ is derived to inflate the GNSS measurement covariance in the state estimator. This turns the usual heuristic adjustment into a convex calibration problem, ensuring non-negativity and interpretability. We seek a time-varying measurement covariance used by a filter (*e.g.*, EKF/UKF) that reflects real GNSS quality:

$$\boldsymbol{R}_k := \sigma^2_{\text{LOS}}\big(1 + \omega_G\,\alpha_k\big)\,\boldsymbol{I}_3, \tag{9}$$

where σ^2_{LOS} denotes the nominal LOS variance determined under favorable conditions, $\alpha_k \in [0,1]$ summarizes the instantaneous GNSS health (with larger values indicating poorer quality), and $\omega_G \geq 0$ scales the overall covariance inflation. The first step in the proposed approach is to compute the LOS baseline, which serves as the reference variance under ideal GNSS conditions (*e.g.*, clear sky, RTK-fixed solution, a large number of satellites). This baseline represents the expected variance when GNSS operates in healthy conditions.

In GNSS multipath/NLOS, the reported position can become biased while still appearing overconfident. The inflation model in (9) reduces overconfidence by increasing $\boldsymbol{R}_k$ as $\alpha_k \to 1$, which in turn reduces the GNSS contribution in the EKF update (smaller Kalman gain for the GNSS measurement). This prevents biased GNSS fixes from pulling the state estimate and allows the filter to rely more on the motion model and the complementary UWB ranges until GNSS quality indicators recover.

We define the set of LOS epochs $\mathcal{L}$ as

$$\mathcal{L} \;=\; \big\{\, k \,|\, \text{epoch } k \text{ satisfies strong LOS conditions} \,\big\},$$

that is, the set of all time indices (epochs) during which the GNSS receiver is assumed to be operating under LOS conditions.

There are two possible approaches for estimating the LOS baseline. The first is an *online/adaptive* strategy, in which the baseline is updated during navigation by continuously monitoring favorable indicators (*e.g.*, RTK-FIXED, low PDOP, a large number of satellites). Epochs meeting these criteria are marked as part of $\mathcal{L}$, based on data collected over intervals of seconds to minutes. However, if the rover never experiences strong LOS conditions during the mission (which is a plausible situation in unstructured agricultural environments) the resulting baseline may be biased. Moreover, this approach requires a robust detection rule to prevent contamination of the baseline with suboptimal data.

To address these limitations, we adopt an *offline calibration* procedure. Specifically, the rover (or receiver) is operated in a known favorable environment (*e.g.*, open sky, RTK-FIXED, many satellites, PDOP ≤ 1.5), and data are collected over several hours. The set of epochs $k \in \mathcal{L}$ satisfying strong LOS conditions is then used to define the LOS baseline as

$$\sigma^2_{\text{LOS}} := \text{median}\big\{\sigma^2_{\text{rep},k}\big\}_{k\in\mathcal{L}}. \tag{10}$$

Having the horizontal $hAcc_k$ and $vAcc_k$ vertical accuracies, we have $\sigma^2_{\text{rep},k}$ as the representative per-epoch variance from the receiver calculated directly by the module:

$$\sigma^2_{\text{rep},k} \;\approx\; \tfrac{1}{3}\Big(hAcc_k^2 + hAcc_k^2 + vAcc_k^2\Big). \tag{11}$$

We construct monotone indicators s_k at time k that increases as conditions worsen, rescaled to $[0,1]$ and clipped:

$$s_k := [\, s_k^{\text{fix}},\; s_k^{\text{dop}},\; s_k^{\text{sv}},\; s_k^{\text{acc}} \,]^\top \in [0,1]^4$$

with Fix-status scores_k^{fix}, Geometry (PDOP) s_k^{dop}, Satellite availability s_k^{sv}, and Accuracy-based s_k^{acc} all mapped to $[0,1]$ and defined as follows:

$$s_k = \begin{cases} s_k^{\text{fix}} = \begin{cases} 0 & \text{RTK-FIXED,} \\ 0.25 & \text{RTK-FLOAT,} \\ 0.5 & \text{DGPS,} \\ 0.75 & \text{3D/2D,} \\ 1 & \text{NO-FIX,} \end{cases} \\ s_k^{\text{dop}} = \text{clip}\left(\dfrac{\text{PDOP}_k - p_{\min}}{p_{\max} - p_{\min}},\, 0,\, 1\right), \quad p_{\min} < p_{\max}, \\ s_k^{\text{sv}} = \text{clip}\left(\dfrac{n_{\text{good}} - \text{num\_sv}_k}{n_{\text{good}} - n_{\text{bad}}},\, 0,\, 1\right), \quad n_{\text{good}} > n_{\text{bad}}, \\ s_k^{\text{acc}} = \text{clip}\left(\dfrac{a_k - a_{\min}}{a_{\max} - a_{\min}},\, 0,\, 1\right), \quad a_k = \sqrt{hAcc_k^2 + vAcc_k^2},\; a_{\min} < a_{\max}. \end{cases} \tag{12}$$

where $\text{clip}(x,a,b) := \min(\max(x,a),b)$. Now we are in a position to define the GNSS measurement health score at epoch k :

$$\alpha_k := \text{clip}\big(w^\top s_k,\, 0,\, 1\big), \tag{13}$$

with $w \in \mathbb{R}^4_{\geq 0}$, $\mathbf{1}^\top w = 1$. Defining the observed inflation

$$\eta_k := \frac{\sigma^2_{\text{rep},k}}{\sigma^2_{\text{LOS}}}. \tag{14}$$

and matching (9) to the observed ratio readily suggests the calibration target

$$\eta_k - 1 \;\approx\; \omega_G\,\alpha_k. \tag{15}$$

which yields $\eta_k - 1 \approx \omega_G(w^\top s_k)$. Letting $\beta := \omega_G\, w \;\in\; \mathbb{R}^4_{\geq 0}$, then $\eta_k - 1 \;\approx\; \beta^\top s_k$. Now given a calibration set C (mix LOS and degraded), we solve the *nonnegative least squares* (NNLS) problem

$$\min_{\beta\geq 0} \sum_{k\in C} \rho\big((\eta_k - 1) - \beta^\top s_k\big), \tag{16}$$

where ρ is the Huber loss. Recovering the desired quantities:

$$\omega_G \;=\; \|\beta\|_1 \;=\; \sum_{i=1}^{4} \beta_i, \qquad w \;=\; \frac{\beta}{\|\beta\|_1}. \tag{17}$$

where $\|\cdot\|_1$ is the ℓ_1 norm. This guarantees $w \geq 0$ and $\mathbf{1}^\top w = 1$, with $\omega_G \geq 0$. Here, $w_{\text{G}} > 0$ is a tunable *GNSS-penalty weight* that controls the inflation of the GNSS covariance under poor (NLOS) satellite conditions. Increasing w_{G} leads to stronger down-weighting of GNSS measurements as $\alpha_k^{\text{GNSS}} \to 1$.

4.2. Adaptive UWB covariance tuning

We adapt the UWB measurement covariance through a learned NLOS severity score. For each UWB packet, the channel statistics are mapped to a reliability indicator $\alpha_k^{\text{UWB}} \in [0,1]$, which scales the measurement variance under degraded conditions. The input feature vector is defined as

$$\mathbf{c}_k = \big[\text{RSS}_k,\; \text{FPR}_k,\; \text{CIK}_k,\; \tau_{r,k}\big]^\top, \tag{18}$$

where RSS denotes the received signal strength, FPR the first-path power ratio, CIK the impulse-response kurtosis, and τ_r the rise time.

The mapping $g : \mathbb{R}^4 \to [0,1]$ is implemented as a lightweight feed-forward neural network:

$$\mathbf{h}_1 \;=\; \text{ReLU}\big(\mathbf{W}_1\,\mathbf{c}_k + \mathbf{b}_1\big), \tag{19}$$

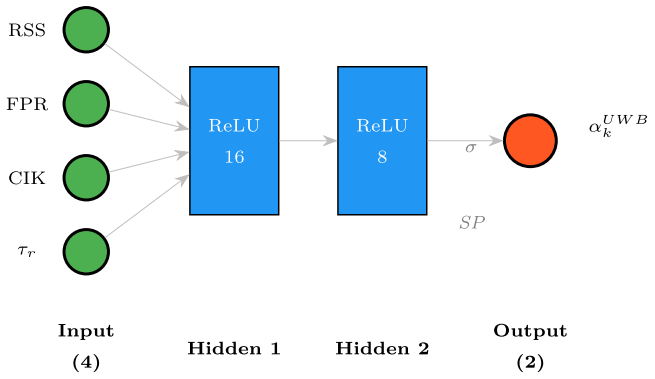

Fig. 3. Proposed neural network architecture with input features RSS, FPR, CIK, and τ_r. The network uses ReLU activation in hidden layers, sigmoid (σ) for α_k^{UWB} output, and softplus (SP) for $q_{b,k}$ output.

Table 3
Sensor specifications.

Sensor Type/Item	Value	Unit
UWB		
Module	DWM1001	
Chip	Decawave DW1000	
Ranging mode	SS-TWR	
Frequency Range	3.5 – 6.5	GHz
Ranging Accuracy	±10	cm
Update rate	10	Hz
GNSS		
Receiver	u-blox ZED-F9P	
Antenna	u-blox ANN-MB1-00	
RTK solution frequency	10	Hz

Table 4
Positioning accuracy comparison between the proposed adaptive EKF and a standard EKF.

Algorithm	Metric	X [m]	Y [m]	Z [m]
EKF Optimal	RMSE	0.051	0.040	0.320
	Std Dev	0.047	0.040	0.135
EKF Standard	RMSE	0.095	0.085	0.640
	Std Dev	0.084	0.084	0.270

$$\mathbf{h}_2 = \mathrm{ReLU}\big(\mathbf{W}_2\,\mathbf{h}_1 + \mathbf{b}_2\big), \tag{20}$$
$$\alpha_k^{\mathrm{UWB}} = \sigma\big(\mathbf{w}_\alpha^{\top}\,\mathbf{h}_2 + b_\alpha\big), \tag{21}$$

with the following architecture (refer to Fig. 3): an input layer with 4 features ($[\mathrm{RSS}, \mathrm{FPR}, \mathrm{CIK}, \tau_r]$), two hidden layers with 16 and 8 units respectively (both with ReLU activation), and an output layer producing $\alpha_k^{\mathrm{UWB}} \in [0, 1]$ through a sigmoid function.

The network was trained on ~10,000 labeled packets collected in mixed LOS/NLOS scenarios. Binary cross-entropy was used as the loss function for LOS/NLOS classification, with Adam optimizer (learning rate 10^{-3}), batch size 64, and 100 training epochs with early stopping. Post-training, temperature scaling was applied to calibrate the sigmoid output on a held-out validation set, thereby improving the probabilistic interpretability of α_k^{UWB} for covariance blending.

To support generalization to agricultural deployments, the training data was designed to cover diverse visibility conditions encountered in field operation (clear LOS, partial occlusions, and intermittent NLOS). While the classifier may not capture all site-specific interference patterns, calibration (via temperature scaling), together with the downstream covariance inflation, is intended to promote conservative behavior under distribution shift by down-weighting measurements when uncertainty is high. This design choice prioritizes robustness over overly confident updates in unseen conditions.

To prevent frame-to-frame flicker, we smooth the learned score via an exponential moving average (EMA):

$$\tilde{\alpha}_k = \lambda\,\alpha_k^{\mathrm{UWB}} + (1-\lambda)\,\tilde{\alpha}_{k-1}, \quad \lambda \in (0, 1]. \tag{22}$$

Instead of unbounded linear inflation, we *blend* between validated LOS/NLOS variances and bound R_k^{UWB}:

$$R_k^{\mathrm{UWB}} = (1-\tilde{\alpha}_k)\,R_{\mathrm{LOS}} + \tilde{\alpha}_k\,R_{\mathrm{NLOS}}, \tag{23}$$
$$R_{\min} \preceq R_k^{\mathrm{UWB}} \preceq R_{\max}. \tag{24}$$

Here R_{LOS} and R_{NLOS} are scalar (or diagonal, per-anchor) variances obtained from a short calibration; $R_{\min}$ and $R_{\max}$ are safety floors/caps (e.g., $R_{\min} = 0.5\,R_{\mathrm{LOS}}$, $R_{\max} = 2\,R_{\mathrm{NLOS}}$).

With the learned-and-stabilized parameters, the EKF uses

$$R_k^{\mathrm{UWB}} = (1-\tilde{\alpha}_k)\,R_{\mathrm{LOS}} + \tilde{\alpha}_k\,R_{\mathrm{NLOS}}, \tag{25}$$
$$R_{\min} \preceq R_k^{\mathrm{UWB}} \preceq R_{\max}. \tag{26}$$

In LOS, small $\tilde{\alpha}_k$ yields $R_k^{\mathrm{UWB}} \approx R_{\mathrm{LOS}}$. In NLOS, R_k^{UWB} inflates toward R_{NLOS}, permitting robust down-weighting of unreliable UWB packets.

4.3. EKF with adaptive noise scaling

The adaptive covariances are integrated into the EKF. At each epoch k, the GNSS and UWB measurement variances are scaled according to the signal quality indicators introduced earlier, with $\mathbf{R}_k^{\mathrm{GNSS}}$ defined in (9) and $R_{i,k}^{\mathrm{UWB}}$ in (24).

Joint covariance. Stacking the GNSS position update (3D) with m UWB ranges, the full measurement covariance is

$$\mathbf{R}_k = \begin{bmatrix} \mathbf{R}_k^{\mathrm{GNSS}} & \mathbf{0}_{3\times m} \\ \mathbf{0}_{m\times 3} & \mathrm{diag}\big(R_{1,k}^{\mathrm{UWB}}, \ldots, R_{m,k}^{\mathrm{UWB}}\big) \end{bmatrix}. \tag{27}$$

For $m = 4$ anchors, $\mathbf{R}_k \in \mathbb{R}^{7\times 7}$.

EKF structure. The filter follows the standard predict–update cycle.

Prediction:

$$\hat{\mathbf{x}}_{k|k-1} = f(\mathbf{x}_{k-1}, \mathbf{u}_{k-1}), \tag{28}$$
$$\mathbf{P}_{k|k-1} = F_{k-1}\,\mathbf{P}_{k-1}\,F_{k-1}^{\top} + Q_{k-1}, \tag{29}$$

where $f(\cdot)$ is the discrete kinematic model (2), F_{k-1} is its Jacobian, and Q_{k-1} is the process noise covariance.

Update:

$$\mathbf{y}_k = \mathbf{z}_k - h(\hat{\mathbf{x}}_{k|k-1}), \tag{30}$$
$$\mathbf{S}_k = H_k\mathbf{P}_{k|k-1}H_k^{\top} + \mathbf{R}_k, \tag{31}$$
$$\mathbf{K}_k = \mathbf{P}_{k|k-1}H_k^{\top}\mathbf{S}_k^{-1}, \tag{32}$$
$$\hat{\mathbf{x}}_{k|k} = \hat{\mathbf{x}}_{k|k-1} + \mathbf{K}_k\mathbf{y}_k, \tag{33}$$
$$\mathbf{P}_{k|k} = (I - \mathbf{K}_k H_k)\,\mathbf{P}_{k|k-1}, \tag{34}$$

where $h(\cdot)$ stacks the GNSS position and UWB range models, and H_k is its Jacobian.

This formulation ensures that the Kalman gain dynamically adapts to the estimated signal quality: when GNSS or UWB degrade, the corresponding entries in $\mathbf{R}_k$ inflate, thereby reducing their contribution to the state update, the whole algorithm is summarized in Algorithm 1.

5. Experimental setup and preliminary validation

The proposed hybrid localization system combines GNSS with UWB and RTK corrections to achieve accurate and robust positioning of the rover, as illustrated in Fig. 4. The UWB subsystem comprises a mobile tag mounted on the rover and four fixed anchors distributed throughout the environment, enabling precise and high-frequency range-based localization. The UWB ranges are obtained using SS-TWR and are produced at 10 Hz. In parallel, the GNSS subsystem employs a ZED-F9P module configured as a base station, which receives RTCM3 correction data from a correction service (*e.g.*, TPOS) via an NTRIP client. These corrections

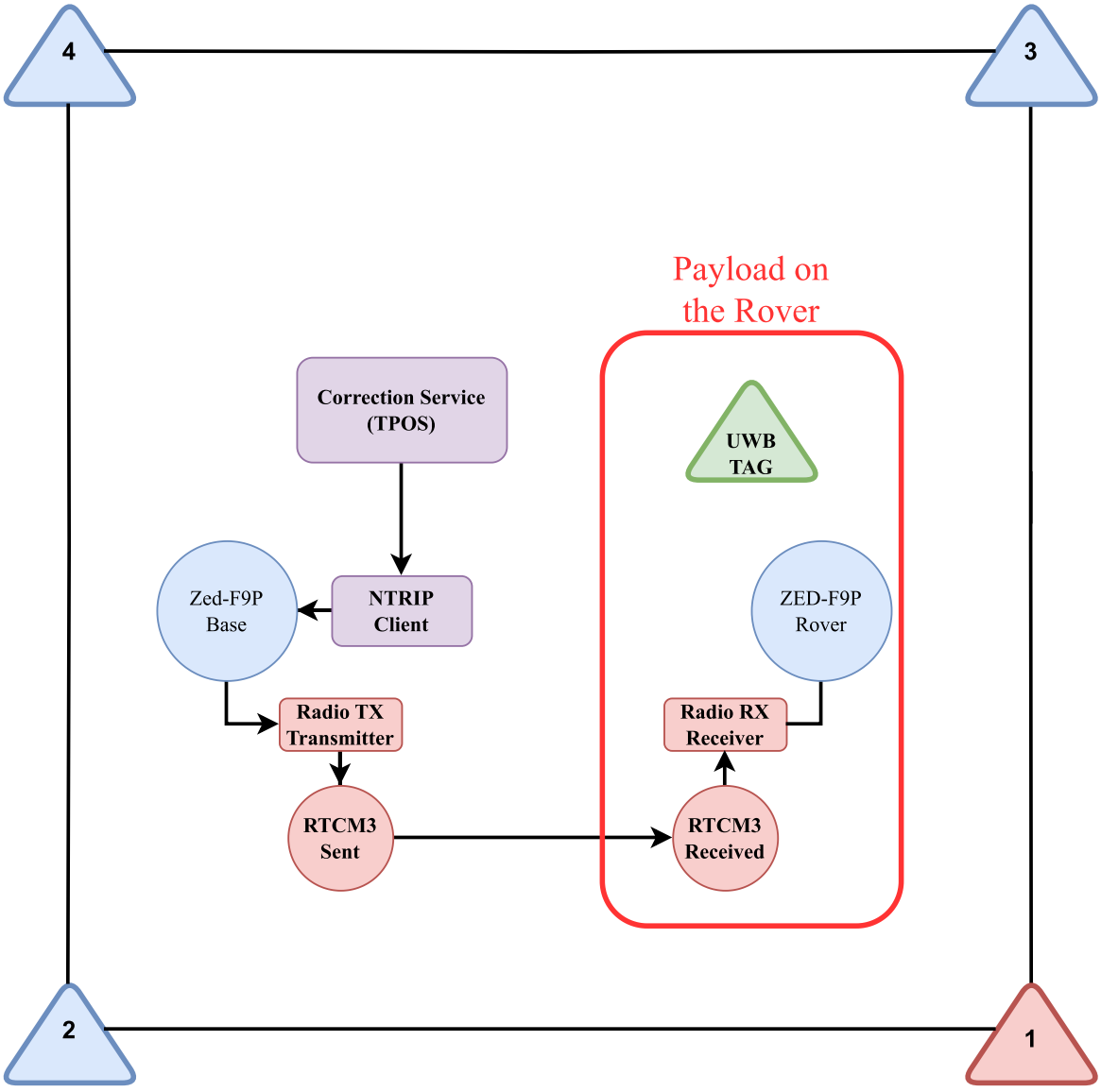

Fig. 4. Experimental system architecture. The setup employs four UWB anchors for ranging and a local ZED-F9P GNSS base station, which receives correction data from the TPOS service via NTRIP. The corrections are broadcast as RTCM3 messages through a radio transmitter to the moving rover. The rover payload consists of a ZED-F9P GNSS receiver and a UWB tag, enabling accurate UWB–GNSS fusion for localization.

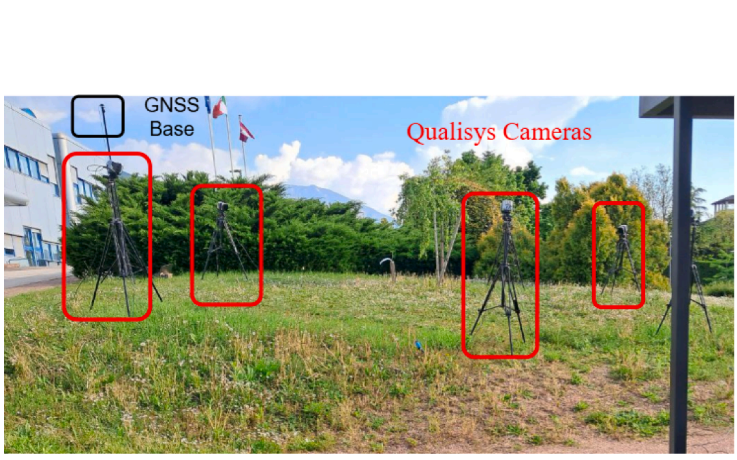

(a) Opti-track experiment.

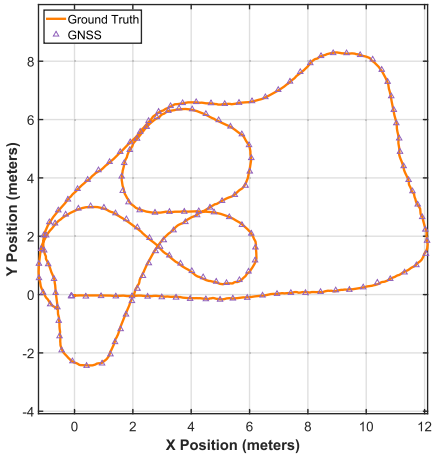

(b) Ground-truth vs RTK in LOS.

Fig. 5. Experimental setup and trajectory: (a) Opti-track system used for ground-truth acquisition; (b) trajectory comparison in the X–Y plane.

Fig. 6. The experimental setup used to assess the performance of the proposed adaptive EKF, with the UWB anchors clearly indicated in the red box. (For interpretation of the references to colour in this figure legend, the reader is referred to the web version of this article.)

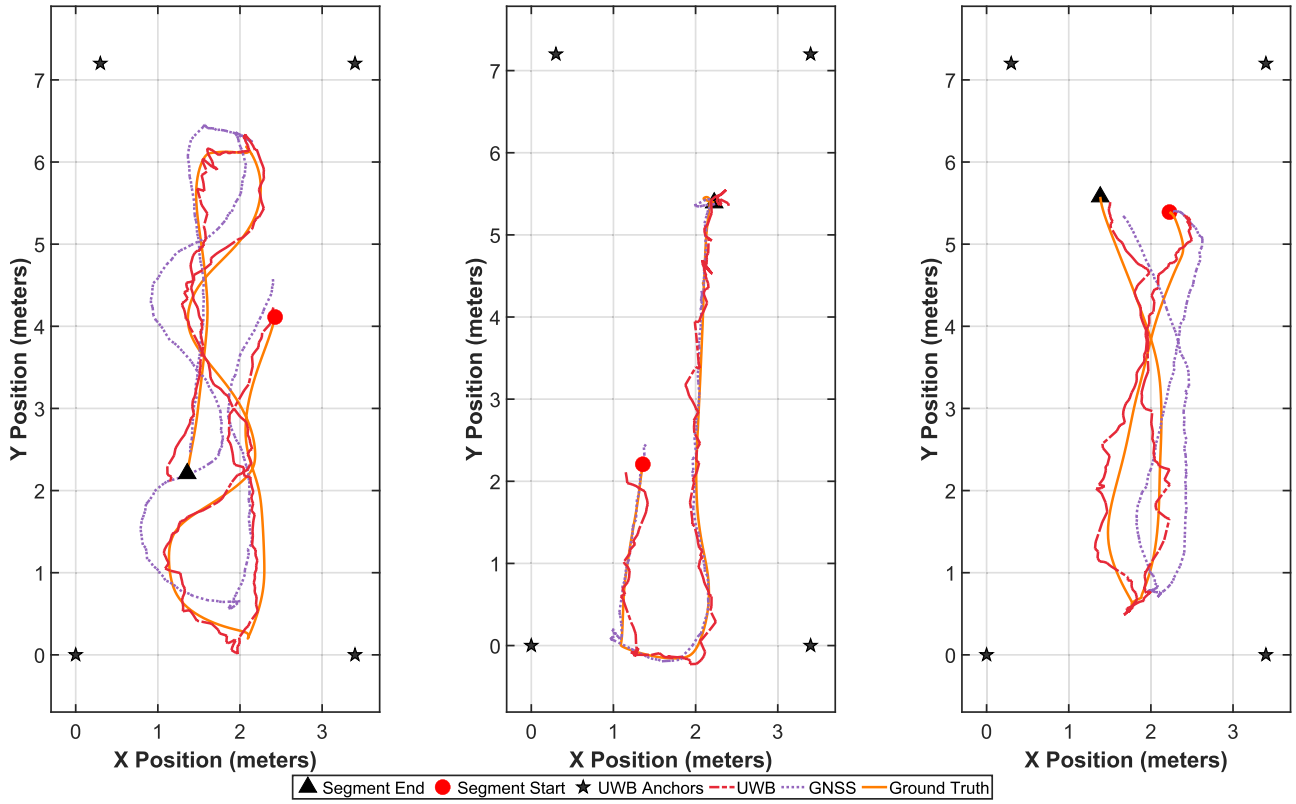

Fig. 7. Trajectory results from three trials comparing GNSS and UWB localization against the ground truth. In Trial 1, GNSS exhibited a noticeable bias relative to the ground-truth path, while UWB provided closer alignment, highlighting systematic GNSS offsets in the test environment. Trial 2, shown in the middle, revealed the opposite effect: GNSS accuracy exceeded that of UWB, demonstrating that under identical conditions GNSS can outperform UWB despite previous results. Trial 3, similar to Trial 1, again showed GNSS bias with UWB providing better agreement with the ground-truth trajectory.

are transmitted wirelessly to the rover through a dedicated radio link, enabling RTK positioning. The rover unit, also equipped with a ZED-F9P receiver and the UWB tag, fuses GNSS and UWB measurements to maintain accurate localization even in partially obstructed or GNSS-degraded environments. Overall, this architecture provides high-frequency, high-accuracy positioning, making it suitable for mobile robotics in agricultural applications, which is summarized in Table 3.

Test environment and NLOS conditions. The evaluation includes an open-sky LOS reference and a partially obstructed agricultural-like environment in which satellite visibility is intermittently degraded by surrounding obstacles and vegetation, inducing multipath and NLOS effects. In this setting, GNSS performance can degrade due to reduced sky view and occasional interruptions in the reception of RTK correction data, while UWB LOS/NLOS conditions vary depending on whether the direct path between the rover tag and each anchor is occluded. These complementary degradation modes motivate the adaptive covariance strategy, which down-weights a sensor when its quality indicators or learned NLOS score indicate reduced reliability.

This first experiment establishes the reference performance of the proposed RTK GNSS subsystem under open-sky (*i.e.*, LOS) conditions. In such scenarios, satellite visibility is unobstructed, and the system is expected to operate close to its declared commercial specifications. Val-

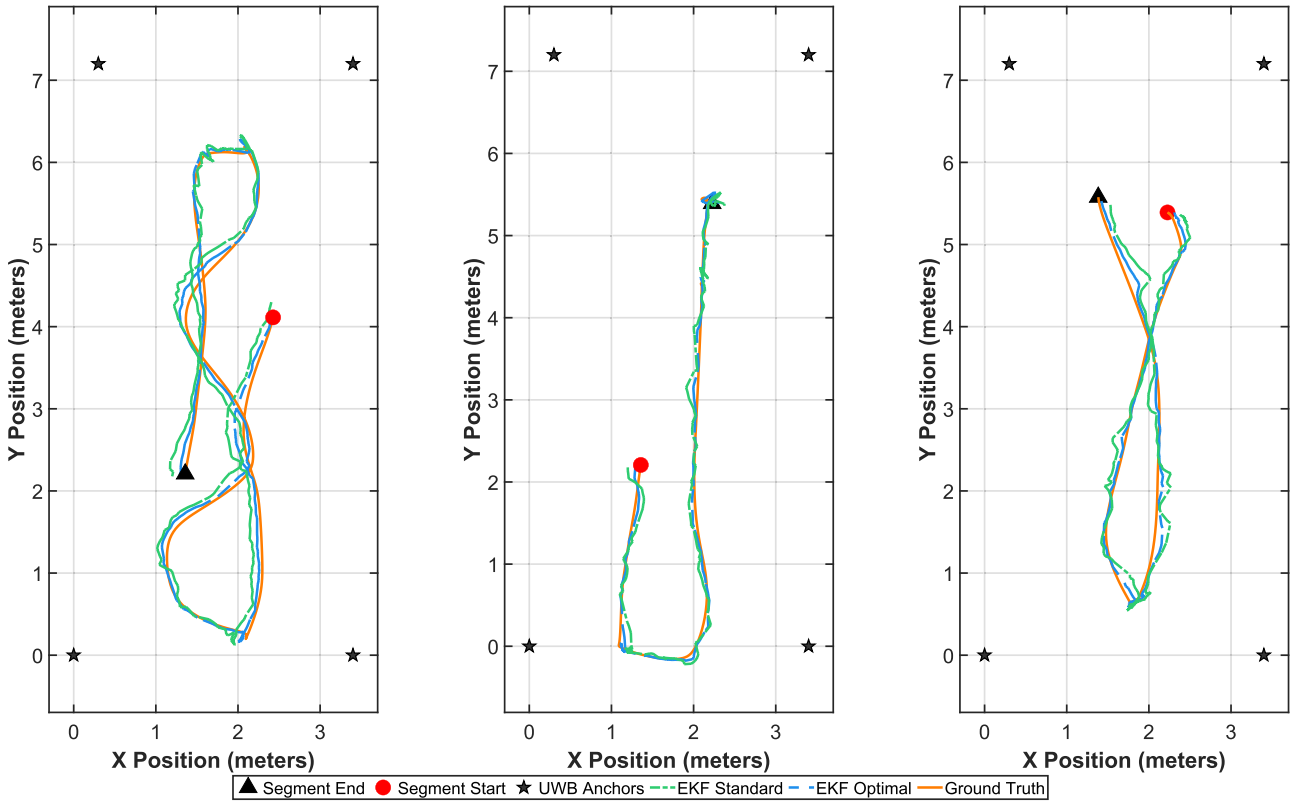

Fig. 8. Visual comparison of the 2D trajectories. The proposed adaptive EKF shows consistently closer agreement with the ground-truth path, effectively reducing the systematic offsets and accumulated drift present in the standard EKF.

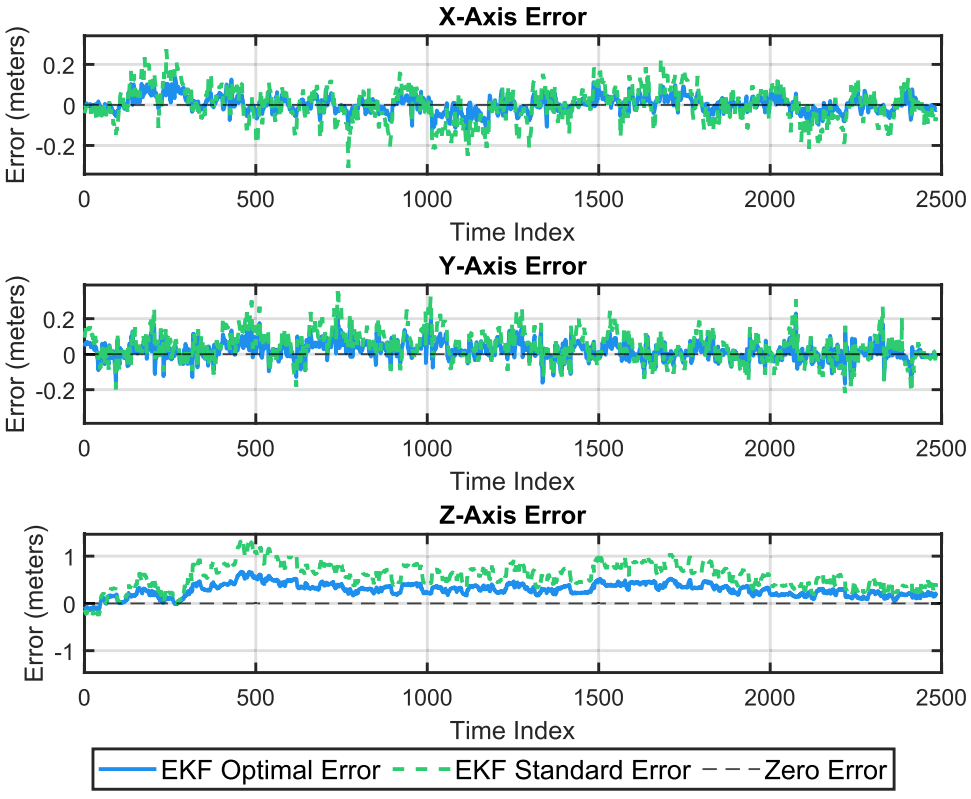

Fig. 9. Component-wise analysis of positioning error over the entire trajectory. The error for the proposed adaptive EKF and the standard EKF are shown for the X-axis (top), Y-axis (middle), and Z-axis (bottom), highlighting the superior accuracy and stability of the proposed method.

Algorithm 1 Adaptive EKF for robust GNSS/UWB fusion.

1. Offline Calibration Phase (Pre-computation)

Calibrate GNSS parameters $(\sigma^2_{\text{LOS}}, \omega_G, w)$ by solving the NNLS problem in Eq. (13) on a calibration set C.

Train the UWB NLOS classification network $g(\cdot)$ on a labeled dataset of channel features $\mathbf{c}_k$.

2. Online Filtering Loop (for each time step k)

// Adaptive Measurement Covariance Estimation

Compute GNSS quality score vector s_k and health score $\alpha_k^{\text{GNSS}} \leftarrow \text{clip}(w^\top s_k, 0, 1)$.

Set GNSS covariance $\mathbf{R}_k^{\text{GNSS}} \leftarrow \sigma^2_{\text{LOS}}(1 + \omega_G\, \alpha_k^{\text{GNSS}})\, \mathbf{I}_3$.

for each UWB anchor $i = 1, \ldots, m$ **do**

  Compute NLOS score $\alpha_{i,k}^{\text{UWB}} \leftarrow g(\mathbf{c}_{i,k})$ and smooth via EMA to get $\tilde{\alpha}_{i,k}$.

  Set UWB variance $R_{i,k}^{\text{UWB}} \leftarrow (1 - \tilde{\alpha}_{i,k})\, R_{\text{LOS}} + \tilde{\alpha}_{i,k}\, R_{\text{NLOS}}$, subject to bounds in Eq. (21).

end for

Construct the joint measurement covariance matrix $\mathbf{R}_k = \text{diag}(\mathbf{R}_k^{\text{GNSS}}, R_{1,k}^{\text{UWB}}, \ldots, R_{m,k}^{\text{UWB}})$.

// EKF Predict-Update Step

Predict the state and covariance to get $\hat{\mathbf{x}}_{k|k-1}$ and $\mathbf{P}_{k|k-1}$.

Update the state and covariance to $\hat{\mathbf{x}}_{k|k}$ and $\mathbf{P}_{k|k}$ using the standard EKF equations with the adaptive measurement covariance $\mathbf{R}_k$.

return $\hat{\mathbf{x}}_{k|k}, \mathbf{P}_{k|k}$

idating this baseline is crucial to ensure that subsequent experiments conducted under degraded conditions (*i.e.*, NLOS) can be properly interpreted. The deployed RTK architecture demonstrates centimeter-level accuracy, achieving a Root Mean Square Error (RMSE) of 0.034 m and a standard deviation of 0.020 m when compared against ground-truth data. These results are confirmed through complementary LiDAR odometry obtained from the FAST-LIO2 algorithm [35], as shown in Fig. 5.

The second experiment setup in Fig. 6 which evaluates the proposed adaptive EKF framework in a controlled, unstructured agricultural-like environment, where satellite visibility is partially obstructed and multipath effects are likely. The experimental setup follows the architecture in Fig. 4 and is tested across three distinct trajectories. Each trajectory includes a direct comparison of GNSS, UWB, and ground-truth positions before applying the fusion algorithm. In Fig. 7, it illustrates that, in certain trials, GNSS yields a trajectory closer to the ground truth, whereas UWB introduces larger deviations. Such complementary error characteristics motivate the proposed adaptive covariance estimation strategy, which adaptively balances sensor contributions based on the changing reliability of GNSS and UWB

6. Experimental results

To evaluate the performance of the proposed adaptive framework, the method was compared against a standard Extended Kalman Filter (EKF) with manually-tuned, static measurement covariances. This static approach is inherently suboptimal, as parameters optimized for one environment (e.g., open sky) yield poor performance in another (e.g., under canopy or dense foliage). In contrast, the proposed adaptive EKF dynamically estimates measurement covariances for both UWB and GNSS to maintain high accuracy across changing conditions.

The quantitative results are summarized in Table 4, with the positioning error for each axis plotted over time in Fig. 9. A visual depiction of the overall trajectory is presented in Fig. 8. The proposed adaptive EKF consistently outperforms the standard EKF, achieving a lower Root Mean Square Error (RMSE) and a smaller standard deviation across all three axes.

Effect of covariance inflation. Table 4 highlights the practical advantage of adaptively scaling measurement covariances. A conventional EKF, tuned with static noise parameters, lacks the flexibility to respond when GNSS accuracy degrades or UWB links transition to NLOS; under such conditions, corrupted observations are weighted too heavily and the state estimate drifts. In contrast, the proposed approach amplifies the measurement covariance, thereby attenuating the Kalman gain, whenever the GNSS health metric or the UWB NLOS classifier indicates unreliable data. The time-series plots in Fig. 9 illustrate this behavior: the standard filter suffers pronounced error peaks and persistent offsets, especially along the vertical axis where GNSS precision is inherently limited, while the adaptive filter keeps errors within a narrower corridor. Quantitatively, the horizontal 2D RMSE drops by 46% (from 0.127 m to 0.065 m) and the vertical RMSE by 50%, confirming that selectively reducing trust in degraded measurements prevents erroneous updates from contaminating the fused solution.

7. Conclusion and future directions

This paper successfully demonstrates an adaptive sensor fusion framework capable of delivering the high-fidelity localization essential for autonomous operations in precision agriculture. By proposing a method that dynamically models sensor uncertainty and actively compensates for UWB NLOS bias, our system achieves centimeter-level accuracy in ideal open-sky conditions. Crucially, it maintains 2D horizontal RMSE below 6 cm in challenging NLOS environments, a performance benchmark that surpasses standard, manually tuned approaches by over 40% in RMSE.

Future research will move beyond the current EKF formulation toward factor-graph optimization, enabling the seamless integration of heterogeneous sensors (GNSS, UWB, IMU, LiDAR/Vision) while incorporating task-specific knowledge, such as crop row geometry. This framework naturally handles asynchronous, multi-rate data, NLOS bias modeling, and anchor calibration, supporting real-time operation through incremental solvers and improving global consistency in long-term missions. Complementary work will address UWB infrastructure design—optimizing anchor placement under field constraints, extending network lifetime via energy-aware policies, and enabling adaptive reconfiguration under canopy dynamics. Finally, a modular, plug-and-play localization payload interfacing with vehicle buses could encapsulate this multi-sensor fusion across diverse agricultural platforms, accelerating deployment of robust and scalable positioning solutions.

CRediT authorship contribution statement

Anas Osman: Writing – review & editing, Writing – original draft, Visualization, Validation, Software, Methodology, Investigation, Data curation, Conceptualization; **Farhad Shamsfakhr:** Writing – review & editing, Writing – original draft, Supervision, Software, Methodology, Investigation, Formal analysis; **Massimo Vecchio:** Writing – review & editing, Writing – original draft, Supervision, Resources, Project administration; **Fabio Antonelli:** Writing – original draft, Resources, Project administration, Funding acquisition.

Data availability

Data will be made available on request.

Declaration of competing interests

The authors declare that they have no known competing financial interests or personal relationships that could have appeared to influence the work reported in this paper

Acknowledgement

This work was partially supported by the AgrifoodTEF project of the Digital Europe Programme (GA #101100622), and the Arrowhead fPVN project of the Chips Joint Undertaking (GA #101111977).

References

[1] D. Radočaj, I. Plaščak, M. Jurišić, Global navigation satellite systems as state-of-the-art solutions in precision agriculture: a review of studies indexed in the web of science, Agriculture 13 (7) (2023) 1417.

[2] A. A. Belal, H. El-Ramady, M. Jalhoum, A. Gad, E. S. Mohamed, Precision farming technologies to increase soil and crop productivity, in: M. Abu-Hashim, F. K. Allouche, A. Negm (Eds.), Agro-Environmental Sustainability in MENA Regions, Cham, Springer International Publishing, 2021, pp. 117–154. https://doi.org/10.1007/978-3-030-51249-6_5

[3] J. Deere, RTK mobile correction signal, 2025. https://www.deere.com/en/technology-products/precision-ag-technology/guidance/mobile-rtk/.

[4] B. Tang, Z. Guo, C. Huang, S. Huai, J. Gai, A fruit-tree mapping system for semi-structured orchards based on multi-sensor-fusion SLAM, IEEE Access 12 (2024) 162122–162130.

[5] Rtkdata, RTKdata delivers centimeter-level accuracy for precision agriculture, 2025. https://www.unmannedsystemstechnology.com/feature/rtkdata-delivers-centimeter-level-accuracy-for-precision-agriculture/.

[6] H. T. S. gaard, I. Lund, Application accuracy of a machine vision-controlled robotic micro-dosing system, Biosyst. Eng. 96 (3) (2007) 315–322. https://doi.org/10.1016/j.biosystemseng.2006.11.004

[7] D. Ahmed, B. M. Imran, M. Churuvija, M. Karkee, An integrated visual servoing framework for precise robotic pruning operations in modern commercial orchard, 2025.

[8] S. Vijayakumar, P. Shanmugapriya, P. Saravanane, T. Ramesh, V. Murugaiyan, S. Ilakkiya, Precision weed control using unmanned aerial vehicles and robots: assessing feasibility, bottlenecks, and recommendations for scaling, NDT 3 (2) (2025).

[9] Y. Guo, et al., A post-processing multipath/nlos bias estimation method based on dbscan, Sensors 24 (8) (2024) 2025–2028. https://doi.org/10.3390/s24082611

[10] Z. Hu, et al., Non-line-of-sight gnss signal classification for urban navigation based on machine learning: comparison and validation, in: Advances in Space ResearchAccessed, 2025, pp. 2025–2028. https://doi.org/10.1016/j.asr.2025.03.018

[11] S. Vélez, J. Valente, T. Bretzel, M. Trommsdorff, Assessing the impact of overhead agrivoltaic systems on gnss signal performance for precision agriculture, Smart Agricul. Technol. 9 (2024) 100664.

[12] Q. Wang, M.S. Chen, G.Q. Wang, K. Li, Y.C. Lin, Z.H. Li, C.Z. Zhang, A novel nlos identification and error mitigation method for uwb ranging and positioning, IEEE Commun. Lett. 28 (1) (2024) 48–52. https://doi.org/10.1109/LCOMM.2023.3340248

[13] Q. Wang, M.S. Chen, J.J. Liu, W.D. Zeng, X. Yan, Y.C. Lin, K. Li, C.Z. Zhang, Parallel deep learning for nlos detection and error mitigation in uwb positioning, IEEE Internet Things J. 12 (20) (2025) 43571–43587. https://doi.org/10.1109/JIOT.2025.3597300

[14] L. Cheng, J. Song, W. Zhao, A hybrid ekf/wufir filter for indoor localization integrating ins and uwb data, IEEE Trans. Network Sci. Eng. 12 (3) (2025) 2266–2276. https://doi.org/10.1109/TNSE.2025.3546918

[15] J. Guo, X. Li, Z. Li, L. Hu, G. Yang, C. Zhao, D. Fairbairn, Multi-GNSS precise point positioning for precision agriculture, 19, 2018. Precision Agriculture.

[16] W. Kowalczyk, T. Hadas, A comparative analysis of the performance of various gnss positioning concepts dedicated to precision agriculture, Reports on Geodesy and Geoinformatics 117 (1) (2024) 20240002.

[17] J. Zhu, H. Zhou, Z. Wang, S. Yang, Improved multi-sensor fusion positioning system based on GNSS/lidar/vision/IMU with semi-tight coupling and graph optimization in GNSS challenging environments, IEEE Trans. Instrum. Meas. 72 (2023) 1–13.

[18] Q. Zhang, Q. Chen, Z. Xu, T. Zhang, X. Niu, Evaluating the navigation performance of multi-information integration based on low-end inertial sensors for precision agriculture, 22, 2021. Precision Agriculture. https://doi.org/10.1007/s11119-020-09747-x

[19] A. N. Sivakumar, M. V. Gasparino, M. Mcguire, V. A. H. Higuti, M. U. Akcal, G. Chowdhary, Lessons from deploying cropfollow : under-canopy agricultural navigation with keypoints, in: IEEE ICRA Workshop on Field Robotics, 2024, pp. 1–6. https://doi.org/10.48550/arXiv.2404.17718

[20] T. Woehrle, A. N. Sivakumar, N. Uppalapati, G. Chowdhary, Metacropfollow: Few-shot adaptation with meta-learning for under-canopy navigation, Technical Report, arXiv preprint, 2024.

[21] W. Z. Kowalczyk, T. Hadas, A comparative analysis of the performance of various gnss positioning concepts dedicated to precision agriculture, Reports on Geodesy and Geoinformatics 117 (2024) 11–20. https://doi.org/10.2478/rgg-2024-0002

[22] A. E. B. Velasquez, V. A. H. Higuti, M. V. Gasparino, A. N. V. Sivakumar, M. Becker, G. Chowdhary, Multi-sensor fusion based robust row following for compact agricultural robots, Field Rob. 2 (2022) 1291–1319. https://doi.org/10.55417/fr.2022043

[23] F. A. A. Cheein, R. Carelli, Agricultural robotics: unmanned robotic service units in agricultural tasks, IEEE Ind. Electron. Mag. 7 (3) (2013) 48–58. https://doi.org/10.1109/MIE.2013.2252957

[24] L. Emmi, E. L. Flécher, V. Cadenat, M. Devy, A hybrid representation of the environment to improve autonomous navigation of mobile robots in agriculture, Precis. Agric. 22 (2) (2021) 524–549. https://doi.org/10.1007/s11119-020-09773-9

[25] J. Liu, W. Gao, Z. Hu, Optimization-based visual-inertial slam tightly coupled with raw gnss measurements, in: 2021 IEEE International Conference on Robotics and Automation (ICRA), IEEE, 2021, pp. 13012–13018. https://doi.org/10.1109/ICRA48506.2021.9561092

[26] D. He, H. Li, J. Yin, Ligo: a tightly coupled lidar-inertial-gnss odometry based on a hierarchy fusion framework for global localization with real-time mapping, 2025.

[27] J. Beuchert, M. Camurri, M. Fallon, Factor graph fusion of raw gnss sensing with imu and lidar for precise robot localization without a base station, in: 2023 IEEE International Conference on Robotics and Automation (ICRA), IEEE, 2023, pp. 1–3.

[28] S. Cao, X. Lu, S. Shen, Gvins: tightly coupled gnss-visual-inertial fusion for smooth and consistent state estimation, IEEE Trans. Rob. 38 (4) (2022) 2004–2021.

[29] C. Villien, B. Denis, UWB-Aided GNSS/INS fusion for resilient positioning in GNSS challenged environments, in: Plans 2023, 2023, pp. 123–145.

[30] M. Tommingas, T. Laadung, S. Varbla, I. Müürsepp, M. M. Alam, UWB And GNSS sensor fusion using ML-Based positioning uncertainty estimation, IEEE Open J. Commun. Soc. 6 (2025) 2177–2189.

[31] U. Albertin, M. Martini, A. Navone, M. Chiaberge, Adaptive robot localization with ultra-wideband novelty detection, Technical Report, arXiv preprint, 2025. https://doi.org/10.48550/arXiv.2505.05903

[32] Z. Zhang, Y. Dong, Y. Wen, H. Yuan, B. Li, Robust pseudorange and carrier phase multipath mitigation with hemispherical map considering the uncertainty, IEEE Sens. J. 24 (7) (2024) 10832–10845. https://doi.org/10.1109/JSEN.2024.3365170

[33] K. Xie, Z. Zhang, High precision uwb localization method for agricultural machinery in unstructured field environment, 2025, p. 117941. https://doi.org/10.1016/j.measurement.2025.117941

[34] W.-N. He, X.-L. Huang, Z. Xu, F. Hu, S. Yu, Adaptive anchor deployment for diverse demands on localization precision, IEEE Trans. Veh. Technol. 73 (12) (2024) 19480–19494. https://doi.org/10.1109/TVT.2024.3439335

[35] W. Xu, J. Lin, D. He, F. Zhang, FAST-LIO2: Fast direct LiDAR-Inertial odometry, IEEE Trans. Rob. 38 (4) (2022) 2053–2073. https://doi.org/10.1109/TRO.2022.3141870